Design and Hardware-in-the-Loop Implementation of Fuzzy-Based Proportional-Integral Control for the Traction Line-Side Converter of a High-Speed Train

Qixiang Yan, Ibrahim Adamu Tasiu *, Hong Chen, Yuting Zhang, Siqi Wu and Zhigang Liu

School of Electrical Engineering, Southwest Jiaotong University, Chengdu 610031, China;
YanaCathy@my.swjtu.edu.cn (Q.Y.); 1101393301@my.swjtu.edu.cn (H.C.); Zhangyuting_137@163.com (Y.Z.);
WUSQ_JTU@163.com (S.W.); liuzg@home.swjtu.edu.cn (Z.L.)
* Correspondence: ibrele@yahoo.com; Tel.: +86-28-8760-3229

check for
updates

Abstract: Power quality is one of many issues affecting the traction power supply system. Prominent among the causes of poor power quality is voltage low-frequency oscillation (VLFO). In this paper, a fuzzy-based PI (FPI) controller to optimize the performance of the traction line-side converter (TLSC) and suppress the effect of VLFO is proposed. Firstly, the mathematical model of China's railway high-speed five single-phase TLSC is developed, and then the FPI control unit is designed based on specific requirements. The fuzzy antecedent and consequence rules were generated based on the expert and previous knowledge of TLSC operation. An offline simulation of the proposed control scheme under different loads and parameters is conducted to verify the designed. To validate the model, the traction power supply system (TPS) is built on the field-programmable gate array (FPGA) real-time digital simulator (FPGA-RTDS), while the FPI control algorithm is load on modeling tech rapid control prototyping (RCP) real-time digital controller (RTDC). Hardware-in-the-loop (HIL), and offline simulation studies between current decoupling (PI) control, sliding mode control (SMC), and the proposed control method confirms in addition to excellent dynamic performance; the proposed method can successfully suppress the effect of VLFO.

Keywords: electric multiple units (EMUs); fuzzy-PI control; hardware-in-the-loop (HIL); high-speed railway; low-frequency oscillation (LFO); StarSim FPGA; traction line-side converter (TLSC)

1. Introduction

Poor control system techniques of train traction line-side converter (TLSC) is primarily believed to be one of the factors creating voltage low-frequency oscillation (VLFO) in high-speed railway, and this phenomenon is increasingly becoming a source of concern in electrified railway operation. The VLFO in the vehicle-grid coupling system (VGCS) can be treated as a continuous stability problem of a large-scale multi-converter system in a specific condition [1]. Scholars are working hard in proposing new control algorithms or changing the current ones hoping at eliminating the power quality issues of the DC-link voltage, and the grid current among them are intelligent controllers. As reported in [2,3], during the last two and half decades, many smart controllers were coupled with optimization algorithms such as genetic algorithm (GA), and neural network (NN) in turning of state observers and control of power electronics.

Control design engineers use fuzzy logic as a powerful tool for simplifying control methodology. It gives them the ability to apply natural human language in describing problems and their solutions. With detailed knowledge of the linguistic variable, a designer can develop a fuzzy control unit without a mathematical model of the system, and this significantly reduces the computation time [4]. It has an

excellent dynamic response, and it can easily overcome the shortcomings of traditional linear control. Another advantage of fuzzy logic control (FLC) is that different types of converters can easily share the same inference rules with little or no modifications [5]. Generally, smart control techniques are suitable for delay/time-varying and nonlinear systems because of their strong robustness, excellent adaptive, and dynamic characteristics, however, limited control precision, high complexity, and lack of complete design tools are some of the issues hindering the development of smart controllers. For such reasons, their use in the field of converter control is still at the infant stage [6]. Despite the enormous challenges associated with intelligent control, some scholars have proposed fuzzy logic solutions for converter operation [7–14].

Electric multiple units or EMUs consist of self-propelled carriages that use electricity as the motive power. Electric traction motors are coupled within one or a number of the wagons of EMUs. An EMU requires no separate locomotive, as it uses traction motors as the primary source of driving power. About 11 years ago, VLFO appeared in China's high-speed railway depot. This phenomenon usually occurs when more than one electric multiple units access the traction power supply system (TPS) at the same time, which is characterized by different amounts of VLFO such as traction network line current, and voltage, and at a particular time, there is a sizeable abnormal fluctuation in the contact network pressure, and the network pressure-flow has a phase difference. The voltage (or current) waveform instantaneous value envelope exhibits low-frequency periodic changes [15,16]. VLFO may cause a severe accident if not detected and addressed in time. It may also trigger the circuit breakers without warning and cause blockage in the TPS, which obstructs the EMUs operation; hence, it's of considerable significance to study the mechanism of VLFO and its suppression methods. This study aims at proposing FPI control to optimize the operation of TLSC and suppress the effect of VLFO [17].

The current mechanism research has not been deepened and is generally believed that the parameters of the EMUs are not matched, but the reasons cannot be clearly explained. At present, there is no mature theory about the mechanism of VLFO. Device mismatch between TPS, and converter control system components are believed to be the primary cause of VLFO by some researchers. Some of them proved that the control strategy of TLSC is the crucial factor in creating VLFO and disturbing the stability of the TPS. Inspired by these studies, it's clear that selecting a good control algorithm can help in reducing the effect of VLFO [17,18]. EMUs usually use current decoupling proportional-integral (PI) control, which can realize the separate control of reactive and active components of the grid side current, and the control objects are all DC quantities [19]. Therefore, the grid side current can be controlled without a static difference. If the set value of the reactive current is adjusted according to the voltage fluctuation of the traction network, the effective control of the LSC can be realized. However, the current decoupling control introduces the delay component of the current, which brings the delay and fluctuation to the dynamic process. Its parameters are also not easy to set and are sensitive to disturbance. PI controller uses K_p to decrease the rise time and K_i to eliminate the steady-state errors but K_p and K_i are deduced by trial and error methods; for this reason, a new design is needed. Another reason is that TLSC is a typical nonlinear multi-variable robust coupling system, and it is sensitive to external disturbances and changes in the system's parameters. The traditional linear control techniques such as PI cannot achieve the ideal control effect. Therefore, it's necessary to introduce a nonlinear intelligent control method into TLSC operation. FLC is the simplest, and more robust among all smart controllers for inverter control application.

As for the existing literature, some studies have proposed auto-disturbance rejection control (ADRC) to enhance the load characteristics of TLSC [16]. A harmonic transfer function was used by Molested et al. to dissect the stability of the TLSC control system and they reached the conclusion that the VLFO stability of VGCS is linked to the control strategy of TLSC [20]. Wang et al. plotted the tendency chart of the system dominant poles to check the influence of TLSC control parameter stability on VLFO [21]. The voltage closed-loop transfer function is driven to test the importance of convert control strategies on VGCS stability and proved beyond a reasonable doubt that the choice of the TLSC control algorithm has a direct impact on the system stability [22]. A repetitive controller was plugged

into the proportional resonant-based (PR) fundamental-frequency (FF) current controller by Yongheng et al. to minimize the converter dead-time harmonics and maintain the control of the FF line current in terms of dynamics [23]. A modified harmonic mitigation method was proposed by Sharifzadeh et al. to cancel all triple harmonics orders in a five-level voltage source inverter, which may easily be extended to any voltage source converter. However, there are still some deficiencies in [20–24]. A new converter control strategy was proposed by Liu et al. to suppress upper harmonics, and though the method has some drawbacks, they succeeded in reducing the distortion rate [25]. Silva suggested a sliding-mode boost-type unity power factor with fewer harmonics contents, and the controller provides bidirectional power flow while controlling both the output voltage and line current [26]. Some researchers have suggested an SMC control solution to improve the performance of the converter [27,28].

To further validate the VLFO suppression effect of the proposed method, the controller was implemented in the hardware-in-the-loop (HIL) simulation platform. The HIL simulation platform of the TPS is built, as shown in Figure 1. It consists of a NI PXle-1071 FPGA-based real-time digital simulator (FPGA-RTDS), NI PXle-1082 real-time digital controller (RTDC) with modeling tech rapid control prototyping (RCP) module, oscilloscope, external host computer, hardware input/output ports, and power supply unit. The NI PXle-1071 is a rugged, rack-mountable, and a 4-slot PXI express backplane with structural designed optimized for maximum usability and flexibility in a wide range of applications, whereas NI PXle-1082 chassis combined a high-performance 8-slot PXI express backplane with high-output power supply, it also ensures a high level of maintainability, resulting in a meager mean time to repair (MTTR). The NI PXle-1082 chassis fully complies with the OXI-5 PXI express hardware specification, offering advanced timing and synchronization features.
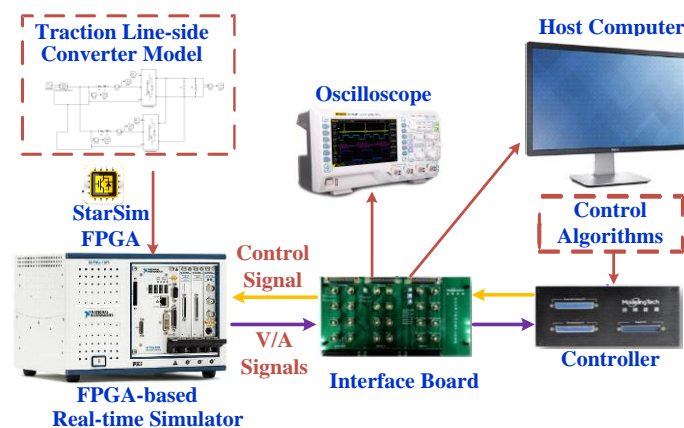

Figure 1. Block diagram of the HIL simulation platform.

FPGA-RTDS and the control algorithm is designed in MATLAB Simulink and downloaded into NI PXle-1082 RTDC using modeling tech StarSim software. StarSim is a LabVIEW-based electromagnetic transient simulation software, mainly for verifying control algorithms and system models. The StarSim express load and convert the StarSim model file into an executable simulation code. The StarSim simulator can download the system model to FPGA without any FPGA programming. The NI PXle-1082 houses the modeling teach RCP controller. The TPS circuit model runs on the FPGA-based real-time simulator, while the control algorithm model runs on the modeling tech RCP controller, thereby forming a closed-loop. The line current, DC-link voltage, and line voltage signals are observed on the oscilloscope and monitor.

The remaining parts of this paper are divided as follows: Section 2 gives China's railway high-speed 5 (CRH5) EMU TLSC circuit model. The FPI controller for single-phase TLSC is designed in Section 3. Section 4 presents the simulation result and verification, and it shows that FPI control can successfully optimize the performance of the TLSC. Section 5 investigated the VLFO suppression effect of the proposed controller. Section 6 validates the simulation results by implementing the design in the HIL simulation platform. Section 7 concludes this paper.

2. Mathematical Model of Single-Phase LSC

Figure 2 shows the main circuit topology of the TPS. Each CRH5 EMU consists of five traction power units. Each traction power unit consists of a dual single-phase TLSC with the same topology, circuit parameters, and control strategy. Considering the VLFO, the EMUs are in the power-up phase of the lift, the inverter and the electric locomotives are in an ideal state, and the impact is negligible. Therefore, it is equivalent to the load resistance. Finally, the equivalent circuit is obtained, as shown in Figure 2, where L_o and R_o are the leakage inductance and resistance. Combination of four insulated gate bipolar transistors (IGBTs) with the following symbols (S_1, S_2, S_3, and S_4) were adopted in building the converter circuit. C_d provides the DC-link capacitance, which plays the role of exchanging reactive power with the leakage inductance of the transformer and replace the car with a purely resistive load R_{load}.
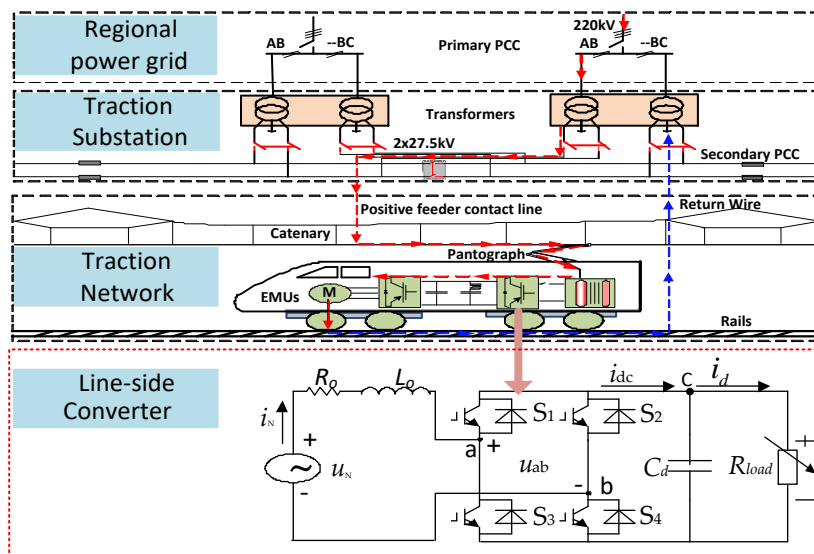

Figure 2. Equivalent circuit of LSC.

The Kirchhoff voltage law is used to calculate the voltages and is applied on the loop marked by the dashed line, and the Kirchhoff current law is applied on the node C. The model of single-phase TLSC can be deduced as follows:

$$L_o \frac{di_N}{dt} + R_o i_N + u_{ab} = u_N$$
$$C_d \frac{du_{dc}}{dt} = i_{dc} - i_d \tag{1}$$

where u_N is the line voltage, i_N is the line current, and u_{ab} is the input voltage. Besides, i_{dc} and i_d represent the current on the DC and load sides. For single-phase systems, it is generally considered $u_n = u_\alpha$ and $i_N = i\alpha$. However, the current and voltage of the alternating current (AC) measurement and the grid side of the rectifier in the two-phase stationary coordinate system are time-varying AC quantities, which is not convenient for control design. Therefore, the two-phase system in the two-phase fixed coordinate system is generally changed into a two-phase system in a two-phase synchronous rotating coordinate system, so that the control amount is changed to a direct current amount.

Let ω be the fundamental voltage frequency of the traction network side, and ϕ be the power factor angle. The primary component of the grid side current and voltage are:

$$u_N = u_{Nd} \sin \omega t + u_{Nq} \cos \omega t$$
$$i_N = i_{Nd} \sin \omega t + i_{Nq} \cos \omega t \tag{2}$$

The input voltage u_{ab} of the rectifier is:

$$u_{ab} = u_{abd} \sin \omega t + u_{abq} \cos \omega t \tag{3}$$

where u_{Nd} and u_{Nq} are the dq component values of the equivalent voltage and i_{Nd} and i_{Nq} are the d-axis and q-axis components of the equivalent current on the traction net side, u_{abd} and u_{abq} are the d-axis and q-axis components of the rectifier input voltage, respectively.

The mathematical model of the AC measurement circuit of TLSC in the dq reference frame is:

$$L_o \frac{di_{Nd}}{dt} = u_{Nd} - R_o i_{Nd} + \omega L_o i_{Nq} - u_{abd}$$
$$L_o \frac{di_{Nq}}{dt} = u_{Nq} - R_N i_{Nq} + \omega L_o i_{Nq} - u_{abq} \tag{4}$$

If we neglect the switching loss of the circuit, the mathematical model of the DC side of single-phase TLSC in the dq reference frame is:

$$\frac{du_{dc}^2}{dt} = -\frac{2u_{dc}^2}{R_d C_d} + \frac{u_{abd}i_{Nd} + u_{abq}i_{Nq}}{C_d} \tag{5}$$

Let us assume the bridge arms of the IGBT are perfect devices. Hence the bridge switching functions are:

$$S_\alpha = \begin{cases} 1, & S_1 \ is \ open \\ 0, & S_3 \ is \ open \end{cases}$$
$$S_\beta = \begin{cases} 1, & S_2 \ is \ open \\ 0, & S_4 \ is \ open \end{cases} \tag{6}$$

11, 10, 01, and 00, are the different logic combination of S_α, S_β, therefore, u_{ab} can be stated as:

$$u_{ab} = (S_\alpha - S_\beta)u_{dc} \tag{7}$$

The decoupled parameters i_d, i_q and e_d, e_q are deduced from the Park transformation matrix by transforming i_N to i_α, and e_N to e_α. i_β and e_β are built by synchronizing the amplitude and frequency of i_N and e_n with a 90° phase lag. Therefore:

$$\begin{bmatrix} e_d \\ e_q \end{bmatrix} = \begin{bmatrix} \cos\omega t & \sin\omega t \\ -\sin\omega t & \cos\omega t \end{bmatrix} \begin{bmatrix} e_\alpha \\ e_\beta \end{bmatrix} \tag{8}$$

$$\begin{bmatrix} i_d \\ i_q \end{bmatrix} = \begin{bmatrix} \cos\omega t & \sin\omega t \\ -\sin\omega t & \cos\omega t \end{bmatrix} \begin{bmatrix} i_\alpha \\ i_\beta \end{bmatrix} \tag{9}$$

where ω is the input voltage frequency, hence (1) can be expressed as:

$$\begin{cases} L_o \frac{di_d}{dt} = -R_o i_d + \omega L_o i_q + e_d - S_d u_{dc} \\ L_o \frac{di_q}{dt} = -R_o i_q - \omega L_o i_d + e_q - S_q u_{dc} \\ C_d \frac{di_q}{dt} = \frac{1}{2}(S_d i_d + S_q i_q) - i_N \end{cases} \tag{10}$$

where S_d and S_q are the converter PWM combinational logic functions that are deduced from S_α and S_β after the decoupling of active and reactive power, and (10) is the TLSC mathematical model.

3. Fuzzy PI Control of a Single-Phase TLSC

The current decoupling control method is used mostly in the converter control of the traction network of the CRH5 type EMU. It mainly consists of a voltage outer loop controller and a current inner loop controller. The PI controller of the voltage control loop ensures that the actual DC voltage tracks its reference, and its output is the reference value of the d-axis current, as shown in Figure 3. The two PI controllers of the current control loop ensure that the q-axis and d-axis currents respectively track their corresponding reference values. Its output is the input signal of the modulation module.
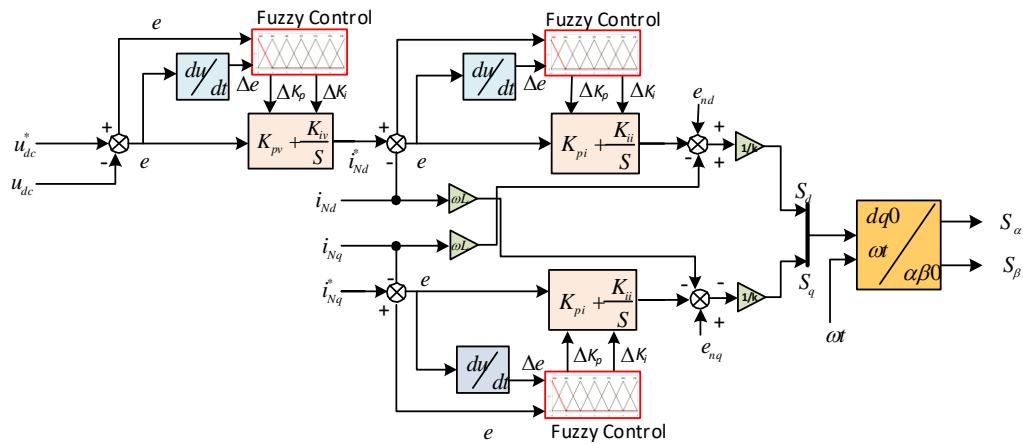
Figure 3. Schematic diagram of the proposed fuzzy PI control method.

The proposed method is the modification of traditional current decoupling control, as shown in Figure 3. The input in the fuzzy PI control is the error *e* and error change rate Δe. The two clear values are first blurred, and then the correction ΔK_p and ΔK_i are inferred by the fuzzy control rule. Finally, defuzzification (clarity) is performed to obtain the value of ΔK_p and ΔK_i.

PI controller generates an output signal consisting of two terms: one proportional to the integral of the error signal and the other proportional to the error signal [29]:

$$u(t) \propto \left[e(t) + \int e(t)dt \right] \tag{11}$$

where *u(t)* and *e(t)* are the control action and error signal in the time domain, respectively.

Therefore:

$$u(t) = K_p e(t) + \frac{K_p}{T_i} \int e(t)dt \tag{12}$$

where T_i is integral time constant, and K_p is the proportional gain.

Taking the Laplace transform of Equation (13) with zero initial condition we get:

$$U(s) = K_p E(s) + \frac{K_p}{T_i} \frac{E(s)}{s} \tag{13}$$

Therefore, the transfer function of PI-controller can be drive as follows:

$$\frac{U(s)}{E(s)} = K_p \left(1 + \frac{1}{T_i s} \right) \tag{14}$$

Hence:

$$\frac{U(s)}{E(s)} = \left(K_p + \frac{K_i}{s} \right) \tag{15}$$

where $K_i = /T_i$, K_p, K_i and T_i are the proportional gain, integral gain, and integral time, respectively.

Let ΔK_p and ΔK_i be the improved values of proportional and integral gain so that the parameter values of the PI control are:

$$\begin{cases} K_p = K_{po} + \Delta K_p \\ K_i = K_{io} + \Delta K_i \end{cases} \tag{16}$$

where K_{po} and K_{io} are the reference values of K_p and K_i, respectively. Equation (16) represents the optimization action of the FPI controller.

The classical design scheme for any FLC consists of the following steps: First, we define the inputs of the plant and control variables, determined the control action to be considered under each system state. Step two is to design the fuzzy inference rule base, established which available fuzzy inference

rule be considered under each condition. Step three is to supply the algorithm and developed the computational unit. The final step is to find rules based on which fuzzy inference can be converted into crisp value [2].

3.1. Fuzzification

Fuzzification is the process of checking the degree of crisp physical value in the appropriate fuzzy set. Membership functions (MFs) degree of each member is obtained and then feed into the inference system for further processing. The general membership function equation is as follows [14]:

$$u(x) = \begin{cases} 1, x = A \\ 0, x \neq A \end{cases} \tag{17}$$

where μ and x are the membership function and the degree of the association in the set of numbers A, respectively. Though any convex shape can be selected for MF, Gaussian, triangular, and trapezoidal functions are turn out to be more suitable with fuzzy logic theoretic and designers than higher-order based functions such as quadratic, or cubic [3]. In this paper, the triangular shape is selected, and the levels chosen for the chosen membership function were, Positive big (PB), Negative big (NB), Positive medium (PM), Negative medium (NM), Positive small (PS), Negative small (NS), and Zero (ZO), as shown in Figure 4 [12].
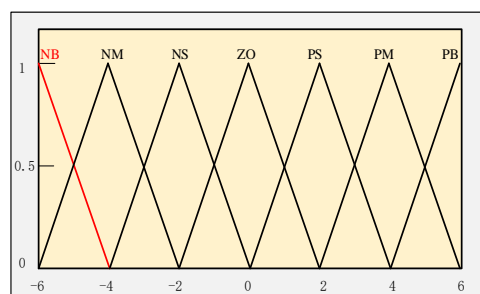

Figure 4. Inputs/outputs membership function plot.

3.2. Fuzzy Inference System (FIS)

The inference engine is the heart of any fuzzy controller, and the inference system generates output based on antecedent-consequence logic. The mapping of the input to the output is the primary function of the inference engine. There are many types of inference systems, and the most popular among them are Sugeno and Mamdani types. The general mathematical expression of Mamdani rule is:

$$R^i : \text{IF} A_{i1}(x_1), A_{i2}(x_2), \ldots, A_{im}(x_m), \text{ THEN Y is } B_i \tag{18}$$

where R is the inference rule, $x_1, x_2, \ldots, x_m$ stand for input variables, $A_{ij}(x_j)(j = 1, 2, 3 \ldots, m)$ is a fuzzy set on x_j, Y is an output variable, B_i is a fuzzy set on Y [3].

Knowledgebase creation is also essential, i.e., inference logic classed in terms of conditions, actions, and statements. Beginning from a verified state (i. e., the situation is "TRUE"), a set of antecedent-consequence rules defined for all the errors are set, which automatically leads to variable output reactions depending on the situation. The knowledge base was sourced and built through experimentation and testing of the LSC and its dynamics [5].

The fuzzy rules were sourced and grouped from human experience and fundamental knowledge about the TLSC operation. About 49 fuzzy inference rules are grouped for both proportional and integral gains. After some tuning, modification, and adjustment cycles, the following rules were deduced and arranged, as shown in Tables 1 and 2. Figure 5 shows the 3-D visualization of inference rules, x-axis indicates the possible values of e, the y-axis shows possible values of Δe, and the z-axis shows next state evaluated by the fuzzy PI controller.

Table 1. The fuzzy control rule of ΔK_p.

	NB	NM	NS	ZO	PS	PM	PB
NB	PB	PB	PB	PB	PS	ZO	NS
NM	PB	PB	PB	PM	ZO	NS	NM
NS	PB	PM	PM	PS	NS	NM	NB
ZO	PS	ZO	ZO	ZO	ZO	ZO	NS
PS	NB	NM	NS	PS	PM	PM	PB
PM	NM	NS	ZO	PM	PB	PB	PB
PB	NS	ZO	PS	PB	PB	PB	PB

Table 2. The fuzzy control rule of ΔK_i.

	NB	NM	NS	ZO	PS	PM	PB
NB	PB	PB	PB	PB	NS	NM	NB
NM	PB	PB	PM	PM	PM	NB	NB
NS	PB	PM	PM	PS	NB	NB	NB
ZO	ZO	ZO	ZO	ZO	ZO	ZO	NM
PS	NB	NB	NB	PS	PS	PM	PB
PM	NB	NB	PM	PM	PB	PB	PB
PB	NB	NM	NS	PB	PB	PB	PB
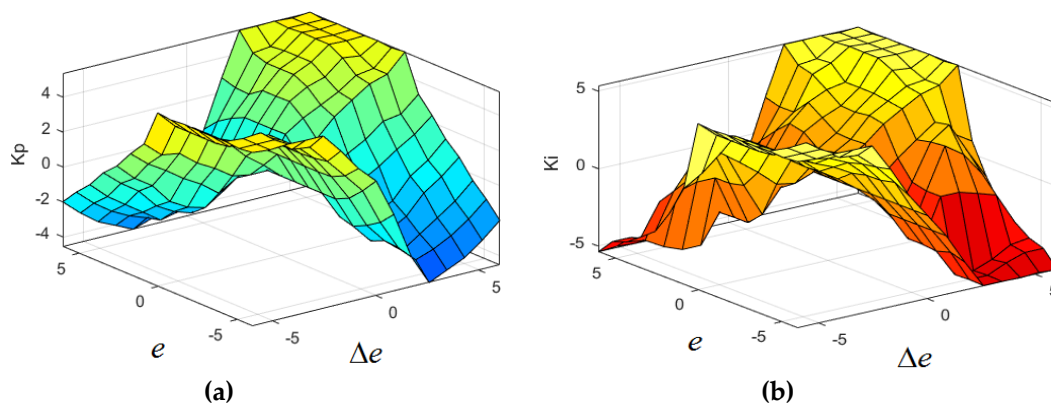
Figure 5. 3D visualization of the fuzzy inference system: (**a**) K_p (**b**) K_i.

3.3. Defuzzification

The process of extracting the crisp values from an antecedent-consequence set is called defuzzification. The gravity method is used as the defuzzification process in this paper. The fuzzy reasoning used in this paper uses the Mamdani reasoning method. It uses the minima to deal with the intersection of fuzzy rule premises. The fuzzy quantity needs to be converted into a precise amount to control the system. The process of converting the fuzzy quantity into an accurate quantity is also called defuzzification or clarity. To obtain an accurate control signal, it is required that the clarity method can well output the calculation result of the membership function. The clarity method adopted in this paper is the "Gravity Method," or "Average Weighted Method." The mathematical expression can be described as [14]:

$$x_o = \frac{\sum_{i=1}^{n} x_i * u(i)}{\sum_{i=1}^{n} u(i)} \tag{19}$$

The method is for each element $x_i(I = 1, 2, 3, \ldots, n)$ in the universe, and it is used as the weighting coefficient of the membership degree u_i of the decision output fuzzy set $x(i) * u(i)$. The average x_0 of the sum of the product and $\sum_{i=1}^{n} x(i) * u(i)$ for membership is calculated. x_o is the result obtained by applying the weighted average method to the fuzzy set. Finally, the output quantization factor

is multiplied by x_0 to accommodate the control requirements so that the actual value of the control amount is available.

4. Simulation and Verification

An offline simulation of the model is implemented in MATLAB/ SIMULINK to verify the effectiveness of the proposed FPI control algorithm. Current decoupling (PI) controller [29], and another excellent nonlinear controller, SMC [26] were also simulated and compared with the proposed FPI control algorithm.

4.1. Simulation of Single-Phase LSC

Figure 6 shows the simulation set-up of four-quadrant TLSC. An offline simulation was carried out and compared. A bipolar carrier PWM algorithm was adopted, and the switching frequency is 350 Hz. The converter parameters are listed in Table A1 as shown in the Appendix A.
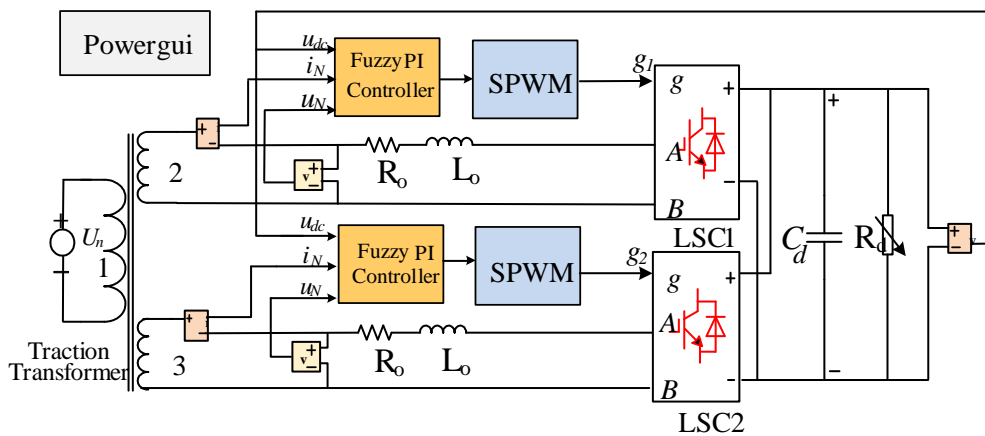
Figure 6. Simulation model of traction LSC.

Figure 7 shows the simulation waveforms of DC-link voltage based on the proposed FPI and the other two controllers. The performance indexes of the DC-link voltages are listed in Table 3. The waveforms of line current and total harmonic distortion (THD) based on the three controllers are as shown in Figure 8. The grid side current and voltage waveforms are as shown in Figure 9.
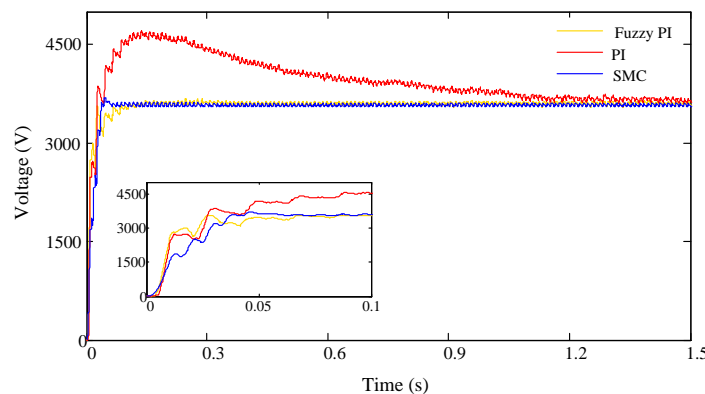
Figure 7. DC-link voltage waveforms.

Table 3. Comparison of performance criteria.

Control	Overshoot	Peak Time	Adjustment Time	Voltage Fluctuation	THD
PI	20.8%	0.23s	1.5s	±40 V	7.89%
SMC	-	-	0.093s	±25 V	6.11%
FPI	-	-	0.085s	±20 V	4.61%

(a)

(b)

(c)
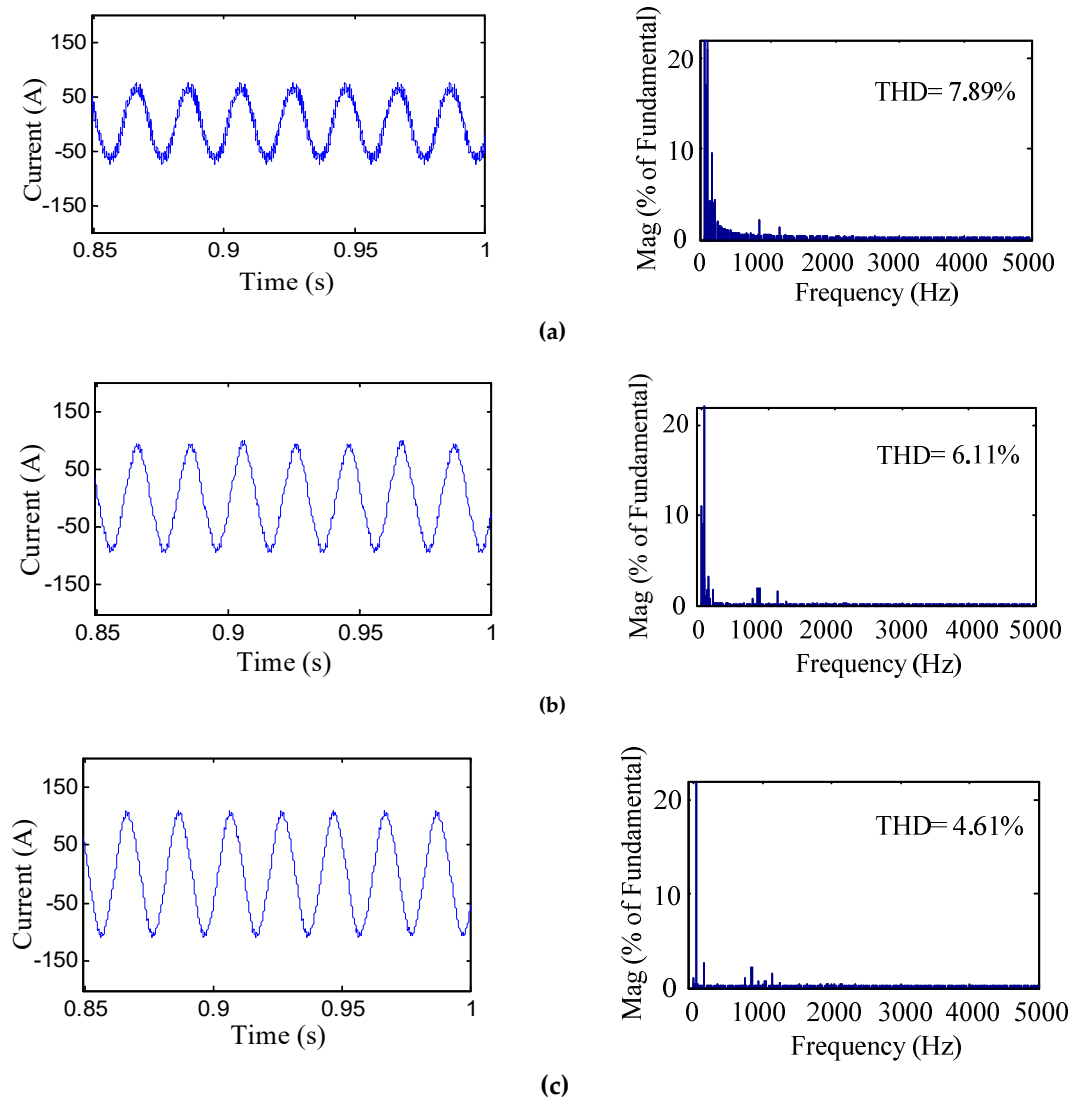
Figure 8. Line current waveforms and THD (**a**) PI (**b**) SMC (**c**) FPI.

Ignoring the recharge stage of the rectifier and the diode rectification phase, the DC side voltage gradually increases from 0 V to 3600 V. When the PI control is put into use, the DC side voltage experiences a relatively long adjustment time to track the reference voltage and has a significant overshoot. When the sliding mode control and FPI control are put into use, the DC voltage quickly followed the reference voltage. Table 3 shows the performance indexes of DC voltages.

Through Fast Fourier Transform (FFT) analysis, the current THD was found to be 7.89%, 6.11%, and 4.61% for PI, SMC, and FPI controllers, respectively, as shown in Figure 8.

(a)

(b)

(c)
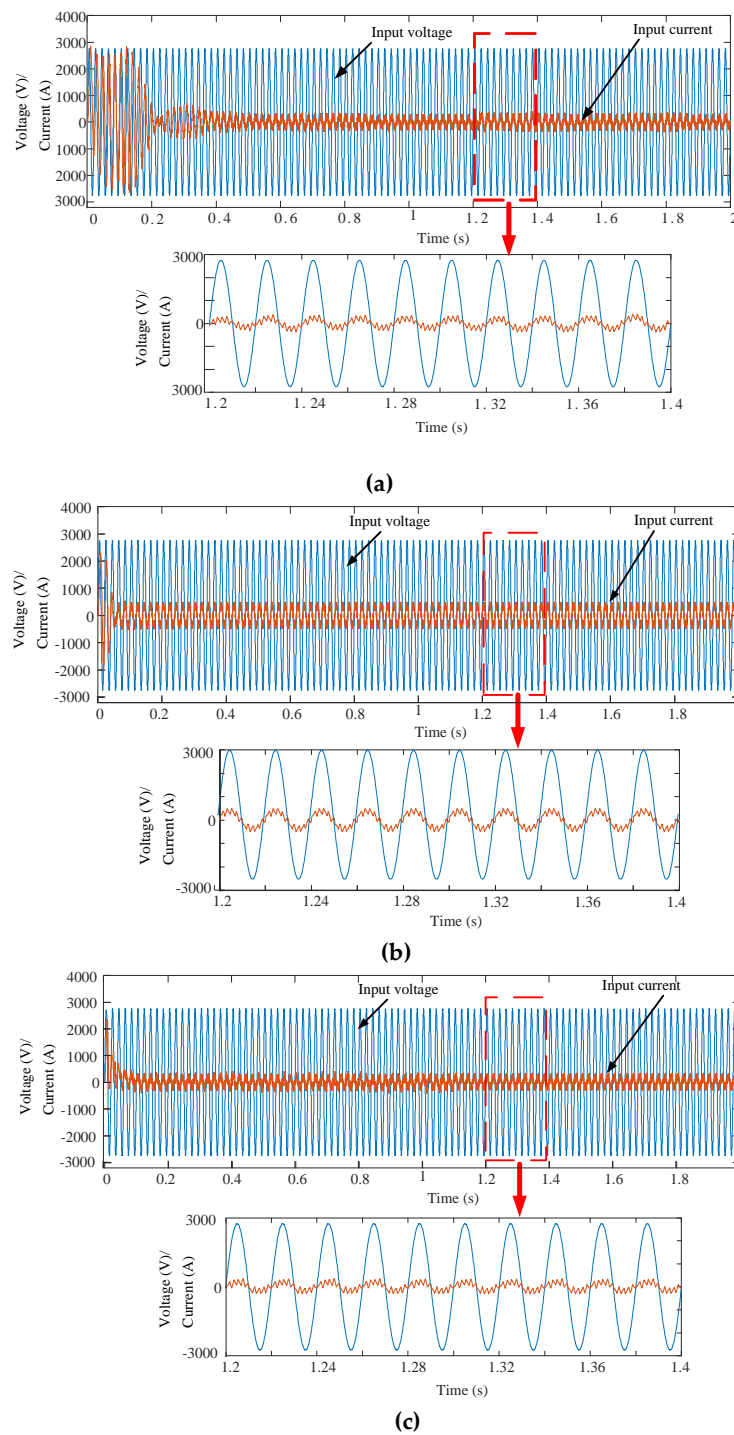
Figure 9. Grid side voltage and current waveforms (**a**) PI (**b**) SMC (**c**) FPI.

The PI controller input current decreases at 0.2 s, and increases again at about 0.2 6 s, before finally settling at 0.38 s, as shown in Figure 9a. The input current and voltage of the three control methods simulated are almost constantly in phase as shown in Figure 9. It was observed that the initial grid current distortion of the FPI controller is negligibly small than the other two methods. Therefore, using the FPI controller in EMUs operation can significantly reduce the input current impact, thereby reducing the damage to equipment. The adjustment time of the FPI controller is also the shortest among the three control methods. The grid current of the two nonlinear controllers is almost invariably in a stable state as shown in Figure 9b,c. From the above results and analysis

we can conclude that the response speed of the system was fantastically improved by the proposed FPI control method, the static and dynamic characteristics of the TLSC was also improved, and the overshoot is significantly reduced to the barest minimum. Hence the proposed FPI controller has better characteristics than SMC and PI controllers.

Figure 10 shows i_d, and i_q simulation waveforms for all three controllers. The d-axis current is stable at 250 A, whereas the q-axis current is stable at 0 A with varying degrees of fluctuation. As can be seen from the figures, PI control has significant variations in the vicinity of the current stability value as compared to FPI control. For SMC, both the q-axis current and the d-axis current quickly stabilized within 0.1s. However, the current widely fluctuates, as shown in Figure 10b. With the proposed FPI control, the current reaches a stable value faster, which implies that the current decoupling effect of FPI is better than the other two controllers.
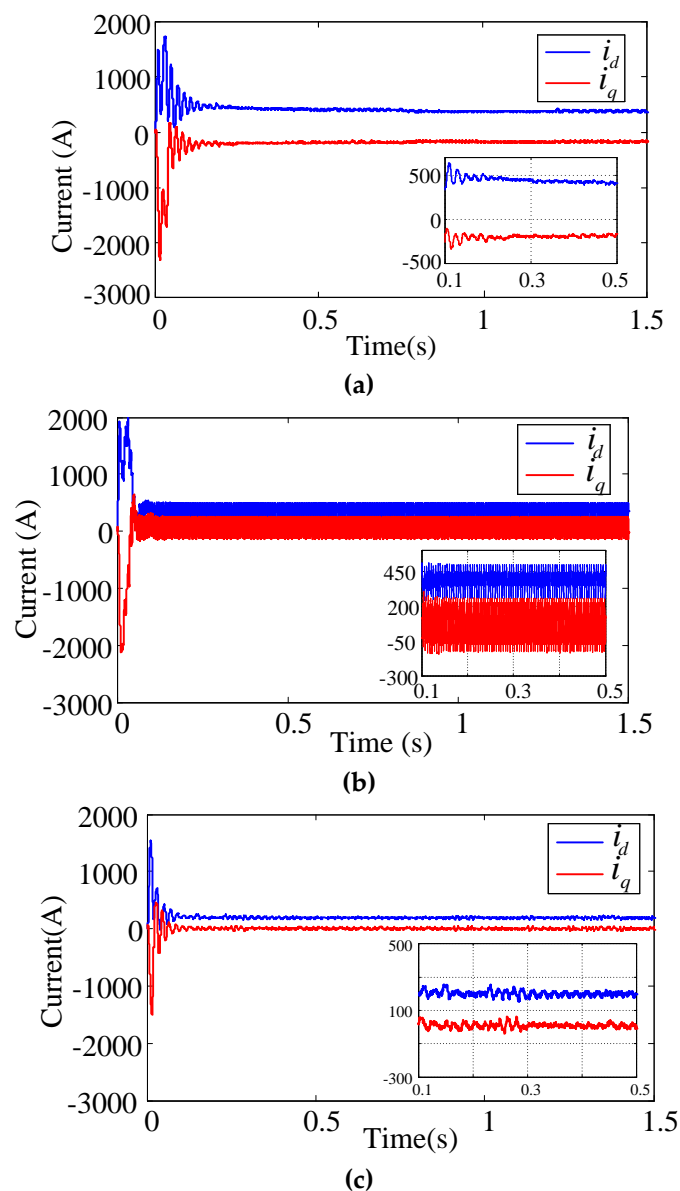
Figure 10. i_d and i_q simulation waveforms (**a**) PI (**b**) SMC (**c**) FPI.

4.2. Sudden-Load-Change Test

At this juncture, it's essential to check the load performance evaluation of the proposed controller. Therefore, a step-changing test is performed. The TLSC equivalent resistant load was initially set at 25 Ω and abruptly changed to 10 Ω at 1.6 s. When the load was kept constant at 25 Ω, both control methods were stable, but when the load suddenly changes at 1.6 s, it was observed that the three control methods experience a voltage drop. The FPI control returns to the reference voltage of 3600 V after 1.8 s, but PI control cannot return to stability after the spike, although the voltage drop of the SMC is small, it can also not be restored to the reference value after the spike, as shown in Figure 11.
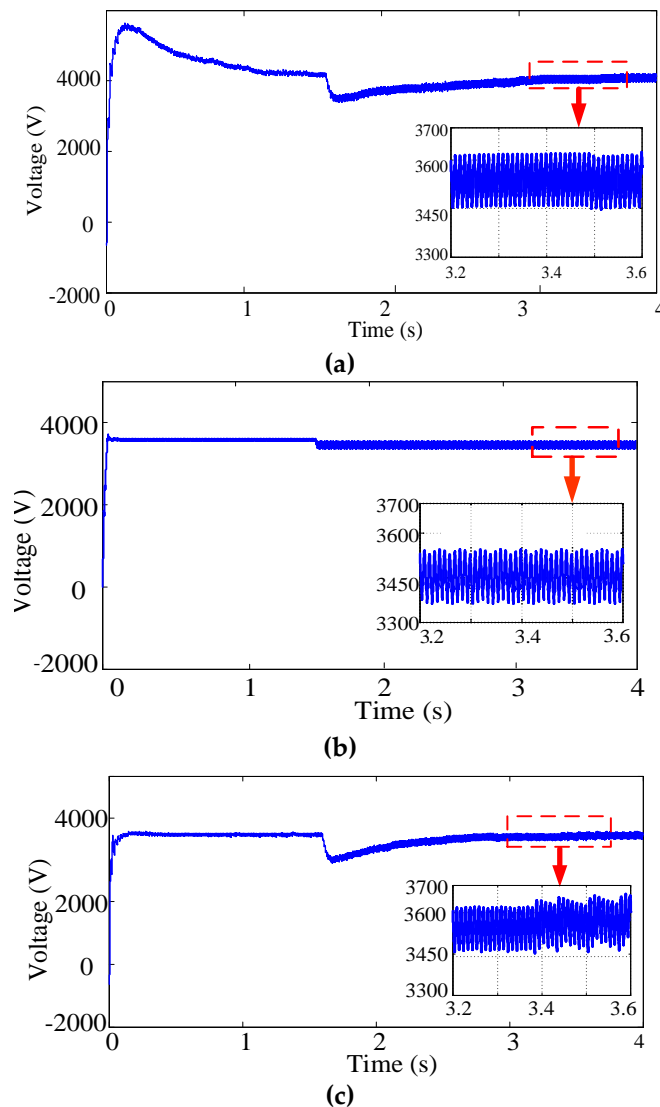
Figure 11. DC-link voltage when the load changes suddenly (**a**) PI (**b**) SMC (**c**) FPI.

Figure 12 shows the waveforms of u_N and i_N of the EMUs single-phase rectifier for the three control methods. As can be seen from the figures, before the load was suddenly changed at 1.6s, the current amplitude is small, about 320 A. After the load abruptly changed, the current amplitude becomes large, about 523 A, which satisfies the power conservation.
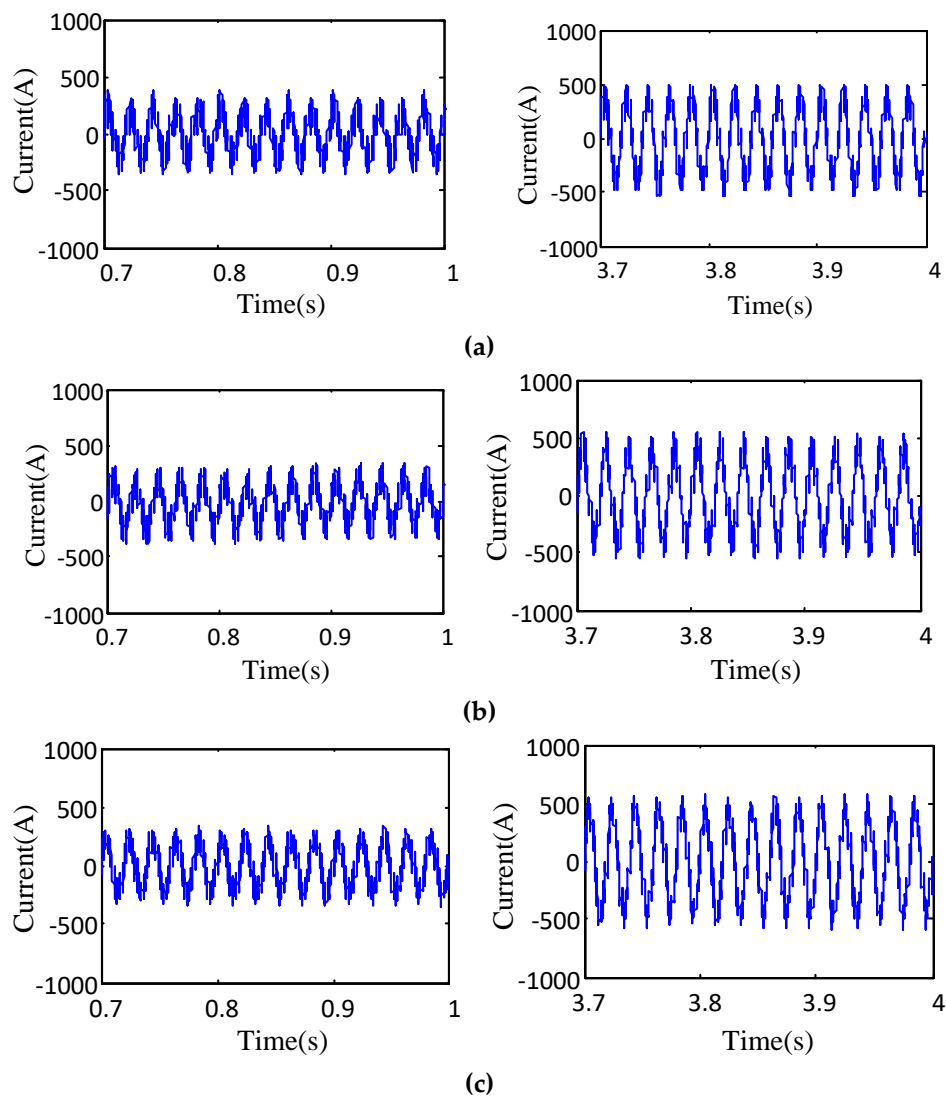
Figure 12. Waveforms of u_N and i_N when the load change suddenly: (**a**) PI (**b**) SMC (**c**) FPI.

Figure 13 shows the q-axis current and d-axis current based on PI control, SMC, and FPI control when the load suddenly changes. It can be observed that at the moment when the load changes, the amplitude of the q-axis current under PI control and SMC decrease and then stabilize at −100 A.
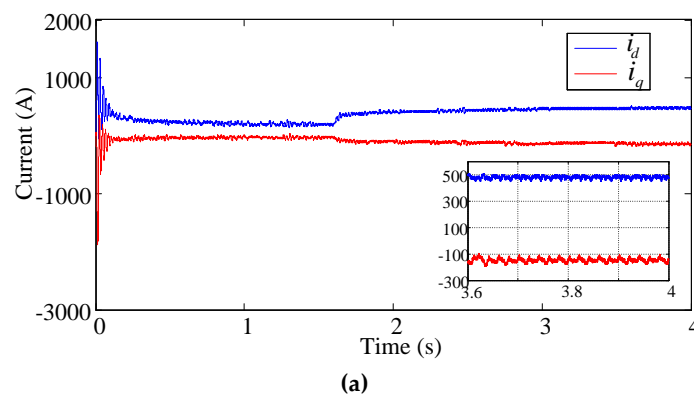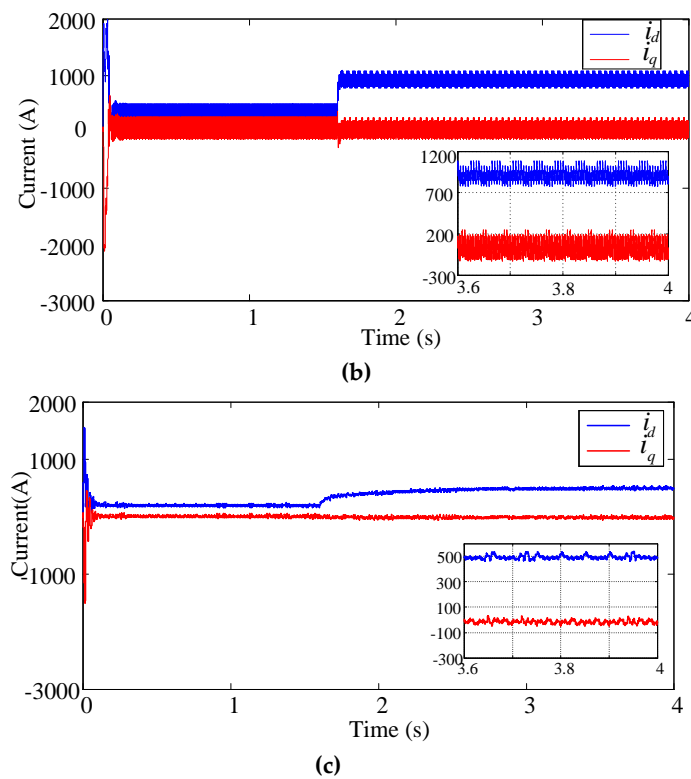

(**a**)

Figure 13. *Cont*.

Figure 13. Waveforms of i_d and i_q when the load change suddenly: (**a**) PI (**b**) SMC (**c**) FPI.

The waveform of d-axis current under PI control rises, and after that stabilizes at 500 A. The q-axis current of FPI control remains stable at 0 A, whereas the q-axis current of PI control and SMC cannot return to 0 A after undergoing load change. Therefore, the power factor cannot reach 1. The FPI controlled d-axis current waveform rises and reached a stable value at a faster speed. In summary, the FPI control can ensure excellent dynamic and static performance. When the load change suddenly, the regular operation of the system can still be guaranteed, and the reference value can be well tracked.

4.3. Variable Grid Inductance Test

We choose grid inductance as a parameter and check its impact on the stability of the VGCS. When the grid inductance L_o varies from 6×10^{-3} to 1×10^{-3} H, the two nonlinear controllers maintained relative stability, as shown in Figure 14b,c, their dynamic performance is unaffected by the change in L_o. On the other hand, the PI controller cannot maintain stability with the increase of L_o as shown in Figure 14a.
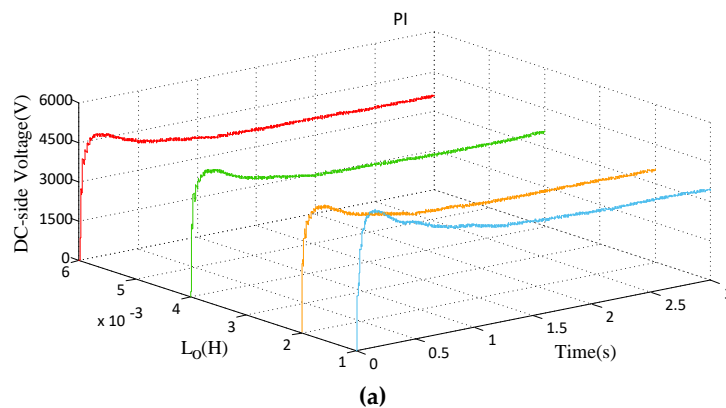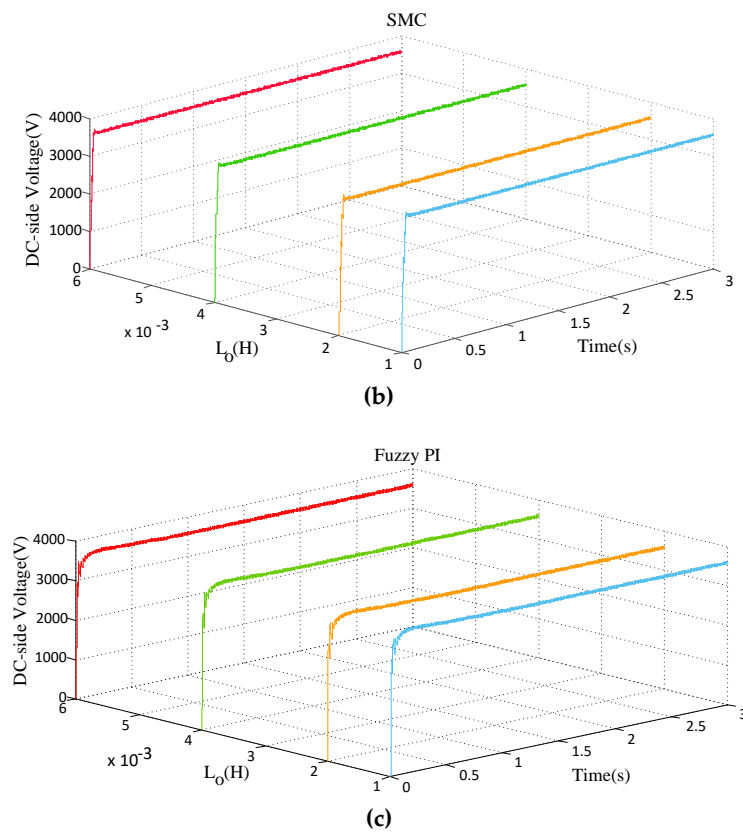

Figure 14. *Cont.*

(b)

(c)

Figure 14. Waveforms of u_d when L_o = 6,4,2 and 1×10^{-3} H: (**a**) PI (**b**) SMC (**c**) FPI.

Figure 15 shows the effect more clearly when $L_o = 1 \times 10^{-3}$ H. It can be seen that both FPI and SMC can track the reference value of 3600 V. The PI controller, on the other hand, cannot follow the reference value of the DC-link voltage when $L_o = 1 \times 10^{-3}$ H. The DC voltage fluctuation of the proposed controller is also the shortest among the three controllers, which shows the superiority of the proposed FPI controller to the system external disturbance.
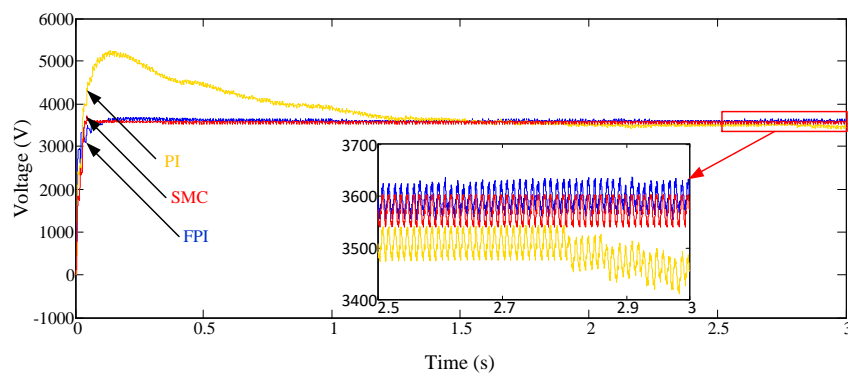
Figure 15. Waveforms of u_d when $L_o = 1 \times 10^{-3}$ H.

4.4. Simulation of Multiple EMUs

To further check the superiority of the proposed controller, the simulation of multiple EMUs connected in the TPS is carried out. CRH5 EMUs were connected in parallel with multiple vehicles and cascaded with the traction network for simulation. To simplify the model, this section uses the Thevenin equivalent voltage source and equivalent impedance values to model the equivalent traction network, as shown in Figure 16. The breaker is a time breaker, and the step module provides an on/off time for the circuit breaker to simulate the situation in which the locomotive is connected to the TPS.

To observed and analyzed the critical impact of the VLFO, all the eight vehicles accessed the TPS at 0s. The performance of the three controllers under test was checked by observing the stability of the VGCS [30,31]. The results obtained are as shown in Figures 17–19.
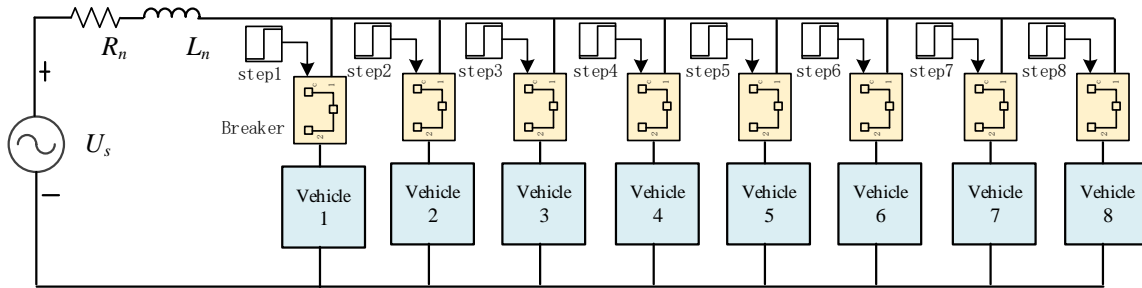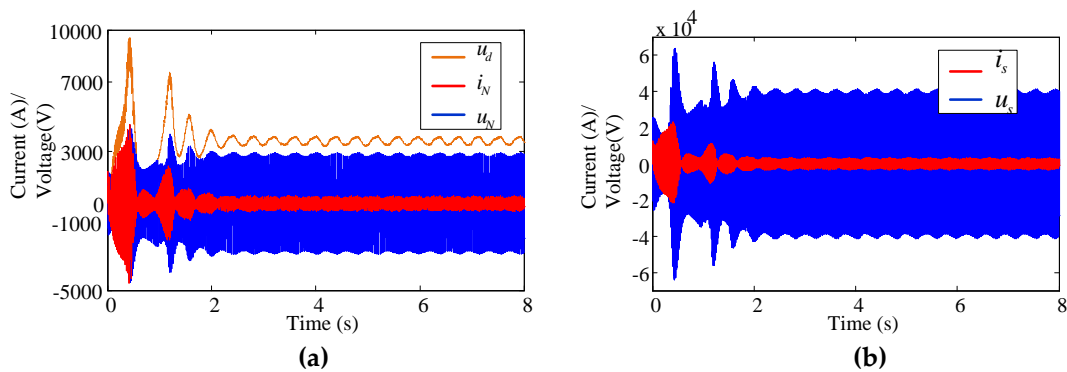

Figure 16. Vehicle-grid coupling system.

Figure 17. PI voltage and current waveforms of multiple EMUs: (**a**) Vehicle side (**b**) Grid side.
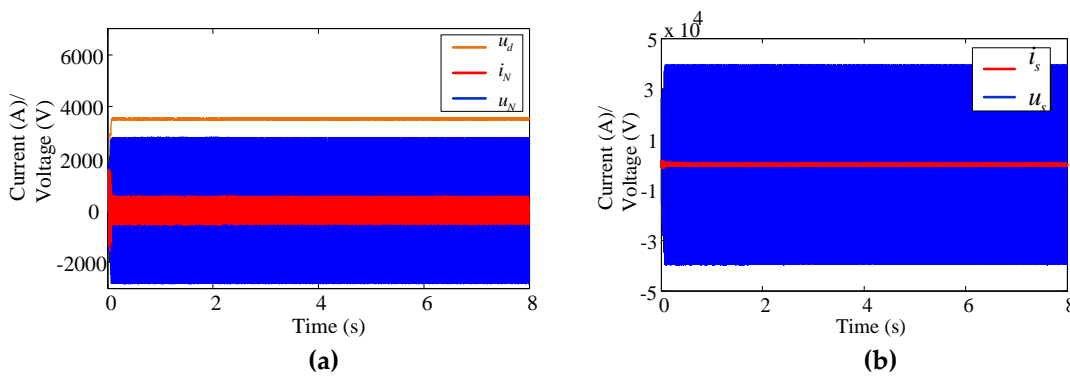

Figure 18. SMC voltage and current waveforms of multiple EMUs: (**a**) Vehicle side (**b**) Grid side.
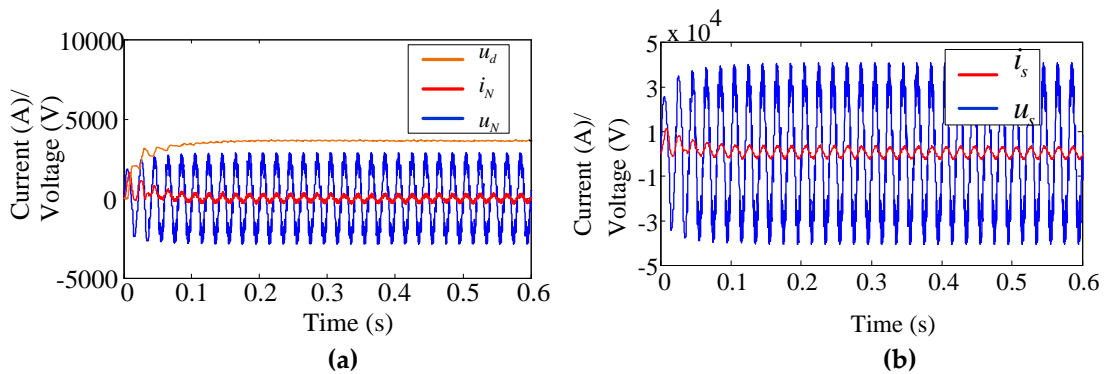

Figure 19. FPI voltage and current waveforms of multiple EMUs: (**a**) Vehicle side (**b**) Grid side.

From Figure 16, it can be observed that when eight vehicles are connected, the current and voltage on the TPS side and the vehicle side both exhibit oscillations, and the steady-state cannot be restored. At this point, the influencing factors from the instability of the vehicle traction power unit exceed the critical value of the system. From Figures 18 and 19, it can be observed that there are no oscillations on both the current and voltage waveforms, and the AC voltage peak on the traction net side is almost invariably stable at 38.89 kV, which indicates that the FPI control algorithm can successfully suppress unstable VLFO.

5. LFO Suppression Test (Worst-Case Scenario)

To further check the suppression effect of the proposed control method on VLFO, a worst-case scenario test was conducted. VLFO usually occurs when the grid inductance L_o is very high, to accord with the practical situation, a VLFO was induced by increasing L_o to the highest maximum value, and the three control methods were put on a test to suppress it. The current and voltage waveforms of the three controllers are as shown in Figure 20.
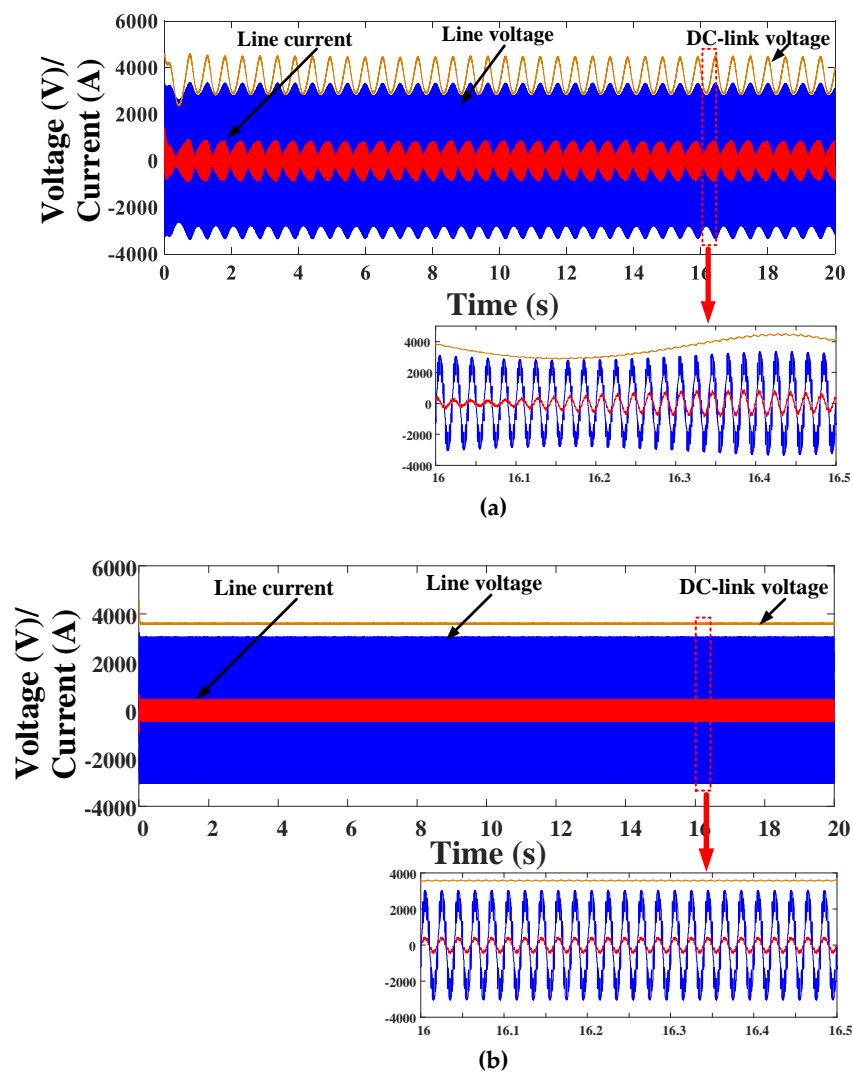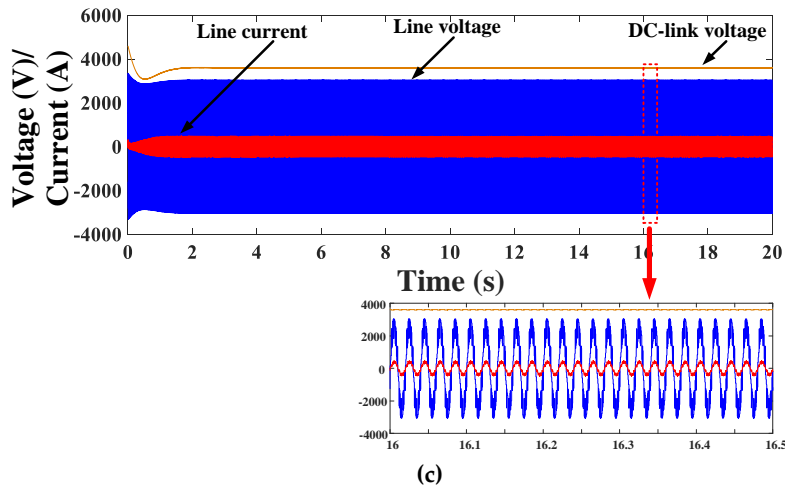

(a)

(b)

Figure 20. *Cont.*

Figure 20. Voltage and current waveforms when $L_o = L_{oMax}$: (**a**) PI (**b**) SMC (**c**) FPI.

From Figure 20a, it can be observed that when the value of the grid inductance is very high, both the voltage and current waveforms exhibit oscillations, and the system cannot maintain stability. A similar test was conducted on the proposed FPI controller and SMC under the same condition, and the two nonlinear controllers effectively suppressed it, as shown in Figure 20a,b. Although the DC voltage of the SMC stabilizes faster than that of FPI, the line current and the DC voltage fluctuations of the proposed controller are the shortest, which validates the superiority of the proposed FPI control on VLFO suppression.

6. HIL Simulation Platform of Traction LSC

To further validate the suppression effect of the proposed FPI Control on the VLFO, the HIL simulation platform was established. It consists of an FPGA-RTDS, Modelling Tech RCP-RTDC module, Oscilloscope, External host computer, Hardware input/output ports, and power supply unit, as shown in Figure 21. The same scenario as in the simulation studies was repeated in the HIL test. The voltage and current waveforms of EMUs LSC were observed. Figures 22–24 depicts the dynamic response of the PI, SMC, and FPI controllers under the same step changes as in the simulation studies, respectively.
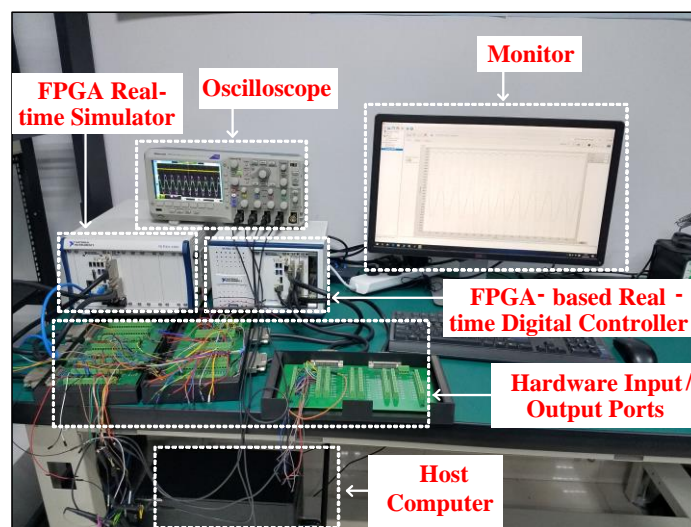

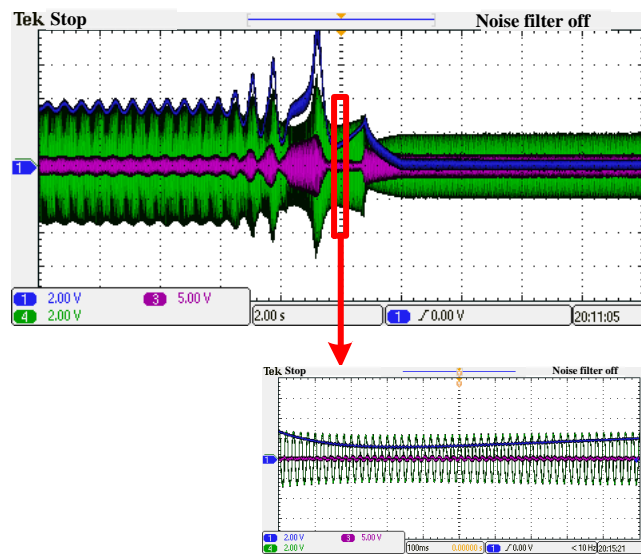**Figure 21.** HIL simulation platform.

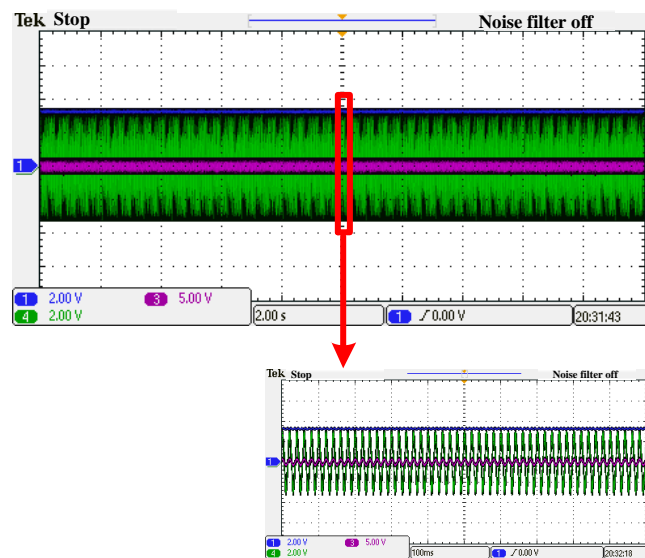**Figure 22.** HIL voltage and current waveforms of PI control.

Figure 23. HIL voltage and current waveforms of SMC control.

Comparing Figures 22–24, one can conclude that when LSC of EMUs is controlled under the proposed FPI control, better quality current with lower fluctuation and THD are generated, and the VLFO was also effectively suppressed. Figure 22 shows that unstable LFO occurred when PI control was put on test on the HIL platform, and when the value of the DC-link voltage is very high, the system collapsed completely. At this point, the DC-link voltage dropped to 0 V. Figures 23 and 24, demonstrated the VLFO suppression effect of the two nonlinear controllers; although the voltage amplitude of SMC is slightly higher than that of FPI, it also maintained stability. Among all three controllers, only FPI tracked the voltage and current waveforms in a near-absolute manner. These improvements were achieved under the condition that the proposed FPI controller is good enough to track a small deviation of the measured parameters from the set-point and automatically takes drastic action. These results validated the suppression effect of FPI control on the VLFO phenomenon and confirmed the superiority of the proposed FPI control scheme.

Finally, to clearly show the contribution of this paper, a comparison between the proposed methods with recent works in the field of FPI is made as shown in Table 4 below.

Table 4. Comparison of the proposed control method with recent works in the field of FPI.

| S/No.	Topic	Control Objectives	Advantages	Disadvantages	Reference
1	Line-side converter Control.	To optimize the performance of the TLSC. To suppress the effect of voltage VLFO.	Smaller overshoot, shorter settling time, and less current THD. Excellent DC-link voltage tracking ability.	Massive memory space occupation, and execution time.	[Proposed control method]
2	Photovoltaic inverter control.	To regulate DC-link voltage.	Improve the steady-state and dynamic performance of the grid-connected PV system. Less harmonic contents.	Complex control structure.	[32]
3	Micro-robot motion control.	To provide 5 degrees of freedom (DOF) for an under actuated bio-inspired helical swimming micro-robot.	Good steady-state error elimination. Robust with an effective trajectory.	It is limited to three helixes as actuators. Only a hydrodynamic force is considered.	[33]
4	Hybrid electric vehicle control.	To enhance fuel economy. To impose a state of charge (SoC) sustainability.	Optimal fuel consumption. Sustainable SoC. Robust with excellent tracking ability.	It cannot guarantee optimality at each time step.	[34]
5	Wind turbine converter control.	To achieve the global optimization for quantization factors k_e and k_{ec}, and scale factors k_{up} and k_{ui}	Less DC voltage overshoot and faster regulation. Excellent speed tracking ability.	It is limited to the maximum power point tracking (MPPT) stage. Low execution time speed.	[35]
6	Power management control.	To minimize the power drawn from the grid. Operate the SOFC within a specific power range.	Smaller overshoot and oscillations. Robust.	The fuzzy control solution is specifically designed for the integral time absolute error (ITAE) performance criteria. The controller might provide different solutions if different performance criteria, such as integral absolute error (IEA) or integral square error (ISE), were used.	[36]
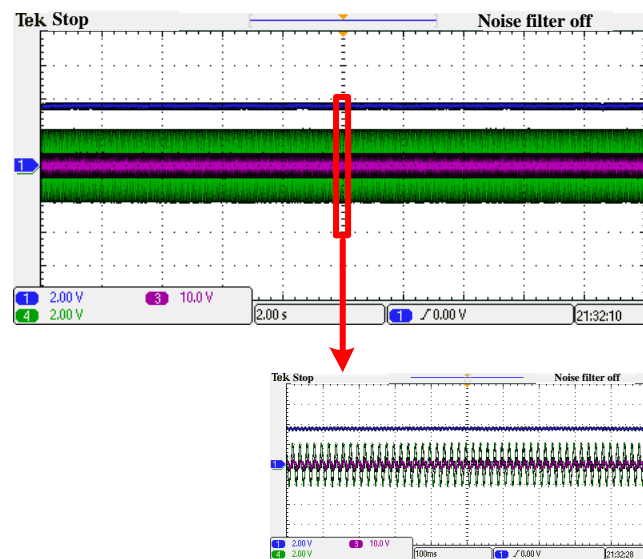
Figure 24. HIL voltage and current waveforms of FPI control.

7. Conclusions

To improve the control performance of the EMUs single-phase TLSC and to suppress the VLFO in the high-speed railway VGCS, the FPI control scheme is proposed. After theoretical analysis, MATLAB, and HIL simulation verifications, the performance of FPI control is compared with PI and SMC. Several conclusions can be drawn:

(1) MATLAB simulation results show that FPI control has better static and dynamic characteristics, such as shorter settling time, less line current THD, and smaller overshoot. When the load changes suddenly, the anti-interference quality of the proposed controller is stronger, and the coupling degree of dq is also better.

(2) A parameter sensitivity test of grid inductance shows that both the proposed FPI and SMC control can track the reference value of the DC-link voltage when the grid inductance varied. While PI, on the other hand, cannot track the reference value of the DC-link voltage under the same condition, this shows the superiority of the proposed FPI controller to the system's external disturbance.

(3) When evaluating multiple EMUs in the reduced-order model of the TPS, the results show that FPI control can guarantee the stability of TLSC and eliminate the low-frequency oscillation more effectively than PI control.

(4) VLFO suppression test conducted under the worst-case scenario confirms the elimination effect of the proposed FPI control scheme on VLFO.

(5) HIL simulation results validate the effectiveness of the proposed FPI control and its superiority in practical applications compared with PI control.

The proposed FPI method can be used for the control of the EMUs TLSC, and the suppression effect on the VLFO is good. Also, fuzzy PI control does not require an accurate mathematical model of the system, which provides greater possibilities for its application. Some advanced work on fuzzy PI control can be studied in the future.

Xipu Campus-10602, Chengdu City-611756, Sichuan Province, People Republic of China, for their immense contribution toward the completion of this research.

Conflicts of Interest: The authors declare no conflict of interest.

Appendix A

The parameters of the traction LSC of CRH5 EMUs and control parameters are listed in Table A1 below.

Table A1. Parameters of the traction LSC of CRH5 EMUs.

System Parameter	Value	Control Parameter	Value
u_s	27.5 kV	K_{iv}	2
L_N	0.0054 H	K_{pv}	1
R_N	0.145 Ω	K_{ii}	1.5
L_o	0.006 H	K_{pi}	8
C_d	0.009 F	b	0.0098
u_d	3600 V	K_1 and K_2	700
R_{load}	25 Ω	e_1 and e_2	19

References

1. Liu, Z.; Wang, Y.; Liu, S.; Li, Z.; Zhang, H.; Zhang, Z. An approach to suppress low-frequency oscillation by combining extended state observer with model predictive control of EMUs rectifier. *IEEE Trans. Power Electron.* **2019**, *34*, 10282–10297. [CrossRef]
2. Tasiu, I.A.; Krushnasamy, V.S.; Juliet, A.V. Analysis of four-quadrant operation and speed control of BLDC motor using fuzzy logic controller in SIMULINK. *Int. J. Appl. Eng. Res.* **2015**, *10*, 15633–15638.
3. Cecati, C.; Ciancetta, F.; Siano, P. A Multilevel inverter for photovoltaic systems with fuzzy logic control. *IEEE Trans. Ind. Electron.* **2010**, *57*, 4115–4125. [CrossRef]
4. So, W.-C.; Tse, C.K.; Lee, Y.-S. Development of a fuzzy logic controller for dc/dc converters: Design, computer simulation, and experimental evaluation. *IEEE Trans. Power Electron.* **2006**, *14*, 293–300.
5. Mattavelli, P.; Rossetto, L.; Spiazzi, G.; Tenti, P. General-purpose fuzzy controller for dc–dc converters. *IEEE Trans. Power Electron.* **1997**, *12*, 79–86. [CrossRef]
6. Han, Y.; Fang, X.; Yang, P.; Wang, C.; Xu, L.; Guerrero, J.M. Stability Analysis of Digital-Controlled Single-Phase Inverter with Synchronous Reference Frame Voltage Control. *IEEE Trans. Power Electron.* **2018**, *33*, 6333–6350. [CrossRef]
7. Kapoor, R.; Tripathi, M.M. Detection and classification of multiple power signal patterns with Volterra series and interval type-2 fuzzy logic system. *Prot. Control. Mod. Power Syst.* **2017**, *2*, 92–101. [CrossRef]
8. Yan, H.; Xu, Y.; Cai, F.; Zhang, H.; Zhao, W.; Gerada, C. PWM-VSI fault diagnosis for a PMSM drive based on the fuzzy logic approach. *IEEE Trans. Power Electron.* **2019**, *34*, 759–768. [CrossRef]
9. Noureldeen, O.; Hamdan, I. A novel controllable crowbar based on fault type protection technique for DFIG wind energy conversion system using adaptive neuro-fuzzy inference system. *Prot. Control. Mod. Power Syst.* **2018**, *3*, 328–339. [CrossRef]
10. Zhu, Y.; Fei, J. Disturbance observer-based fuzzy sliding mode control of PV grid-connected inverter. *IEEE Access* **2018**, *6*, 21202–21211. [CrossRef]
11. Soliman, M.A.; Hasanien, H.M.; Azazi, H.Z.; El-Kholy, E.E.; Mahmoud, S.A. An adaptive fuzzy logic control strategy for performance enhancement of a grid-connected PMSG-based wind turbine. *IEEE Trans. Ind. Inform.* **2019**, *15*, 3163–3173. [CrossRef]
12. Bhosale, R.; Agarwal, V. Fuzzy logic control of the ultracapacitor interface for enhance transient response and voltage stability of a DC microgrid. *IEEE Trans. Ind. Appl.* **2019**, *55*, 712–720. [CrossRef]
13. Hong, Y.-Y.; Liu, M.-J. Optimized interval type-II controller-based STATCOM for voltage regulation in power systems with photovoltaic farm. *IEEE Access* **2018**, *6*, 78731–78739. [CrossRef]

14. Hannan, M.A.; Ghani, Z.A.; Hoque, M.M.; Ker, P.J.; Hussain, A.; Mohamed, A. Fuzzy logic inverter controller in photovoltaic applications: Issues and recommendations. *IEEE Access* **2019**, *7*, 24934–24955. [CrossRef]

15. Menth, S.; Meyer, M. Low-frequency power oscillation in electric railway systems. *Elek. Bahnen* **2006**, *104*, 216–221.

16. Zhang, G.; Liu, Z.; Yao, S.; Liao, Y.; Xiang, C. Suppression of low-frequency oscillation in traction network of high-speed railway based on auto-disturbance rejection control. *IEEE Trans. Transp. Electrif.* **2016**, *2*, 244–255. [CrossRef]

17. Liu, Z.; Zhang, G.; Liao, Y. Stability research of high-speed railway EMUs and traction network cascade system considering impedance matching. *IEEE Trans. Ind. Appl.* **2016**, *52*, 4315–4326. [CrossRef]

18. Liu, Z.; Hu, X.; Liao, Y. Vehicle-grid system stability analysis based on norm criterion and suppression of low-frequency oscillation with MMC-STATCOM. *IEEE Trans. Transp. Electrif.* **2018**, *4*, 757–766. [CrossRef]

19. Liu, Z.; Li, J.; Li, Z. Research on current decoupling control system based on dual closed-loop PI control. *Process. Autom. Instrum.* **2018**, *33*, 35–58.

20. Mollerstedt, E.; Bernhardsson, B. Out of control because of harmonics-an analysis of the harmonic response of an inverter locomotive. *IEEE Trans. Control. Syst.* **2000**, *20*, 70–81.

21. Wang, H.; Wu, M.; Sun, J. Analysis of low-frequency oscillation in electric railways based on small-signal modeling of vehicle-grid system in dq frame. *IEEE Trans. Power Electron.* **2015**, *30*, 5318–5330. [CrossRef]

22. Han, Z.; Tang, L.; Li, W. Causal analysis and resolution of the voltage instability between AC drive electric locomotive and power supply network. *J. China Railw. Soc.* **2011**, *33*, 25–28.

23. Yang, Y.; Zhou, K.; Wang, H.; Blaabjerg, F. Analysis and mitigation of dead-time harmonics in the single-phase full-bridge PWM converter with repetitive controllers. *IEEE Trans. Ind. Appl.* **2018**, *54*, 5343–5354. [CrossRef]

24. Sharifzadeh, M.; Vahedi, H.; Portillo, R.; Franquelo, L.G.; Al-Haddad, K. Selective harmonic mitigation based self-elimination of triplen harmonic for single-phase five-level inverters. *IEEE Trans. Power Electron.* **2019**, *34*, 86–96. [CrossRef]

25. Liu, Z.; Xiang, C.; Wang, Y.; Liao, Y.; Zhang, G. A model-based predictive direct power control for traction line-side converter in high-speed railway. *IEEE Trans. Ind. Appl.* **2017**, *53*, 4934–4943. [CrossRef]

26. Silva, J.F. Sliding-mode control of boost-type unity-power-factor PWM rectifiers. *IEEE Trans. Ind. Electron.* **1999**, *46*, 594–603. [CrossRef]

27. Alsumiri, M.; Li, L.; Jiang, L.; Tang, W. Residue Theorem based soft sliding mode control for wind power generation systems. *Prot. Control. Mod. Power Syst.* **2018**, *3*, 247–258. [CrossRef]

28. Ayyarao, T.S. Modified vector controlled DFIG wind energy system based on barrier function adaptive sliding mode control. *Prot. Control. Mod. Power Syst.* **2019**, *4*, 34–41. [CrossRef]

29. Mevai, M.; Naouar, M.W.; S-Belkhodja, I.; Monmasson, E. An adaptive PI controller design for DC-link voltage control of single-phase grid-connected converters. *IEEE Trans. Ind. Electron.* **2019**, *66*, 6241–6249.

30. Liu, Z.; Geng, Z.; Wu, S.; Hu, X.; Zhang, Z. A passivity-based control of Euler-Lagrange model for suppressing voltage low-frequency oscillation in high-speed railway. *IEEE Trans. Ind. Inform.* **2019**. [CrossRef]

31. Liu, Z.; Liu, S.; Li, Z.; Tasiu, I. A novel approach based on extended state observer sliding mode control to suppress low-frequency oscillation traction network. *IEEE Access* **2019**, *7*, 52440–52454. [CrossRef]

32. Zeb, K.; Islam, S.U.; Din, W.U.; Khan, I.; Ishfaq, M.; Busarello, T.D.C.; Ahmad, I.; Kim, H.J. Design of fuzzy-PI and fuzzy-sliding mode controllers for single-phase two-stages grid-connected transformerless photovoltaic inverter. *Electronics* **2019**, *8*, 520. [CrossRef]

33. Pourmand, M.J.; Taghaei, S.; Vatankhah, R.; Arefi, M.M. An underactuated bio-inspired helical swimming microrobot using fuzzy-PI controller with novel detection method for 5-DOF micromanipulation. *Designs* **2018**, *2*, 18. [CrossRef]

34. Zhang, F.; Liu, H.; Hu, Y.; Xi, J. A supervisory control algorithm of hybrid electric vehicle based on adaptive equivalent consumption minimization strategy with fuzzy PI. *Energies* **2016**, *9*, 919. [CrossRef]

35. Xiao, Y.; Zhang, T.; Ding, Z.; Li, C. The study of fuzzy proportional-integral controllers based on improved particle swarm optimization for permanent magnet direct drive wind turbine converters. *Energies* **2016**, *9*, 343. [CrossRef]

36. Sukumar, S.; Marsadek, M.; Ramasamy, A.; Mokhlis, H.; Mekhilef, S. A fuzzy-based PI controller for power management of a grid-connected PV-SOFC hybrid system. *Energies* **2017**, *10*, 1720. [CrossRef]